

# Dopant-Driven Positive Reinforcement in Ex-Solution Process: New Strategy to Develop Highly Capable and Durable Catalytic Materials

Ji-Soo Jang, Jun Kyu Kim, Kyeounghak Kim, Wan-Gil Jung, Chaesung Lim, Sangwoo Kim, Dong-Ha Kim, Bong-Joong Kim,\* Jeong Woo Han,\* WooChul Jung,\* and Il-Doo Kim\*

The ex-solution phenomenon, a central platform for growing metal nanoparticles on the surface of host oxides in real time with high durability and a fine distribution, has recently been applied to various scientific and industrial fields, such as catalysis, sensing, and renewable energy. However, the high-temperature processing required for ex-solutions (>700 °C) limits the applicable material compositions and has hindered advances in this technique. Here, an unprecedented approach is reported for low-temperature particle ex-solution on important nanoscale binary oxides. WO<sub>3</sub> with a nanosheet structure is selected as the parent oxide, and Ir serves as the active metal species that produces the ex-solved metallic particles. Importantly, Ir doping facilitates a phase transition in the WO<sub>3</sub> bulk lattice, which further promotes Ir ex-solution at the oxide surface and eventually enables the formation of Ir particles (<3 nm) at temperatures as low as 300 °C. Low-temperature ex-solution effectively inhibits the agglomeration of WO<sub>3</sub> sheets while maintaining well-dispersed ex-solved particles. Furthermore, the Ir-decorated WO<sub>3</sub> sheets show excellent durability and H<sub>2</sub>S selectivity when used as sensing materials, suggesting that this is a generalizable synthetic strategy for preparing highly robust heterogeneous catalysts for a variety of applications.

Supported catalysts, in which metal nanoparticles (NPs) are distributed on oxide supports, are widely used in a variety of industrial processes, including in catalysis,<sup>[1]</sup> sensing,<sup>[2]</sup> and renewable energy.<sup>[3]</sup> To improve the reactivity, cost-effectiveness, and durability of catalysts, decreasing their particle size to ensure uniform dispersion on the support and to suppress their aggregation during operation, particularly at high temperatures (>500 °C) is of utmost importance. Thus far, not only conventional impregnation and coprecipitation approaches but also numerous new synthesis and dispersion techniques have been actively studied.<sup>[4]</sup>

Recently, the spontaneous growth of metal NPs on the surface of a host oxide, called “ex-solution,” has attracted much attention as a new route to obtain supported catalysts.<sup>[5]</sup> It is based on the phenomenon that certain cations in a complex oxide lattice selectively precipitate on the surface when the oxide is partially reduced at high temperatures.<sup>[6]</sup> In particular, when catalytically active and highly reducible

transition metals are used as dopants, metal NPs can be uniformly dispersed on the oxide surface with only a single heat treatment.<sup>[7]</sup> Furthermore, the metal NPs produced by ex-solution are strongly bound to the host oxide and thus have excellent thermal and chemical stability.<sup>[8,9]</sup> Accordingly, thanks to these advantages, the ex-solution process is now being applied in high-temperature chemical and electrochemical applications, such as solid oxide fuel cells,<sup>[10]</sup> electrolyzers,<sup>[11]</sup> and oxidation catalysts.<sup>[12]</sup>

However, the high-temperature heat treatment required to obtain ex-solved particles is a substantial barrier that significantly limits the use of this process in a wider range of applications. To achieve high catalytic reactivity, not only the metal particles but also the oxide support should have a large specific surface area, whereas at high temperatures, sintering between the oxide supports often occurs, deactivating the catalysts. Therefore, it is necessary to develop a strategy for activating the ex-solution process at a temperature low enough that the nanoscale oxide supports do not aggregate. In this regard, Irvine et al. proposed facilitating the extrusion of B-site cations

Dr. J.-S. Jang  
Department of Chemical and Environmental Engineering  
Yale University  
New Haven, CT 06520-8286, USA

J. K. Kim, S. Kim, D.-H. Kim, Prof. W. Jung, Prof. I.-D. Kim  
Department of Materials Science and Engineering  
Korea Advanced Institute of Science and Technology (KAIST)  
291 Daehak-ro, Yuseong-gu, Daejeon 34141, South Korea  
E-mail: wjung@kaist.ac.kr; idkim@kaist.ac.kr

K. Kim, C. Lim, Prof. J. W. Han  
Department of Chemical Engineering  
Pohang University of Science and Technology (POSTECH)  
77 Cheongam-ro, Nam-gu, Pohang 37673, South Korea  
E-mail: jwhan@postech.ac.kr

W.-G. Jung, Prof. B.-J. Kim  
School of Materials Science and Engineering  
Gwangju Institute of Science and Technology (GIST)  
123 Cheomdangwagi-ro, Buk-gu, Gwangju 61005, South Korea  
E-mail: kimbj@gist.ac.kr

 The ORCID identification number(s) for the author(s) of this article can be found under <https://doi.org/10.1002/adma.202003983>.

DOI: 10.1002/adma.202003983

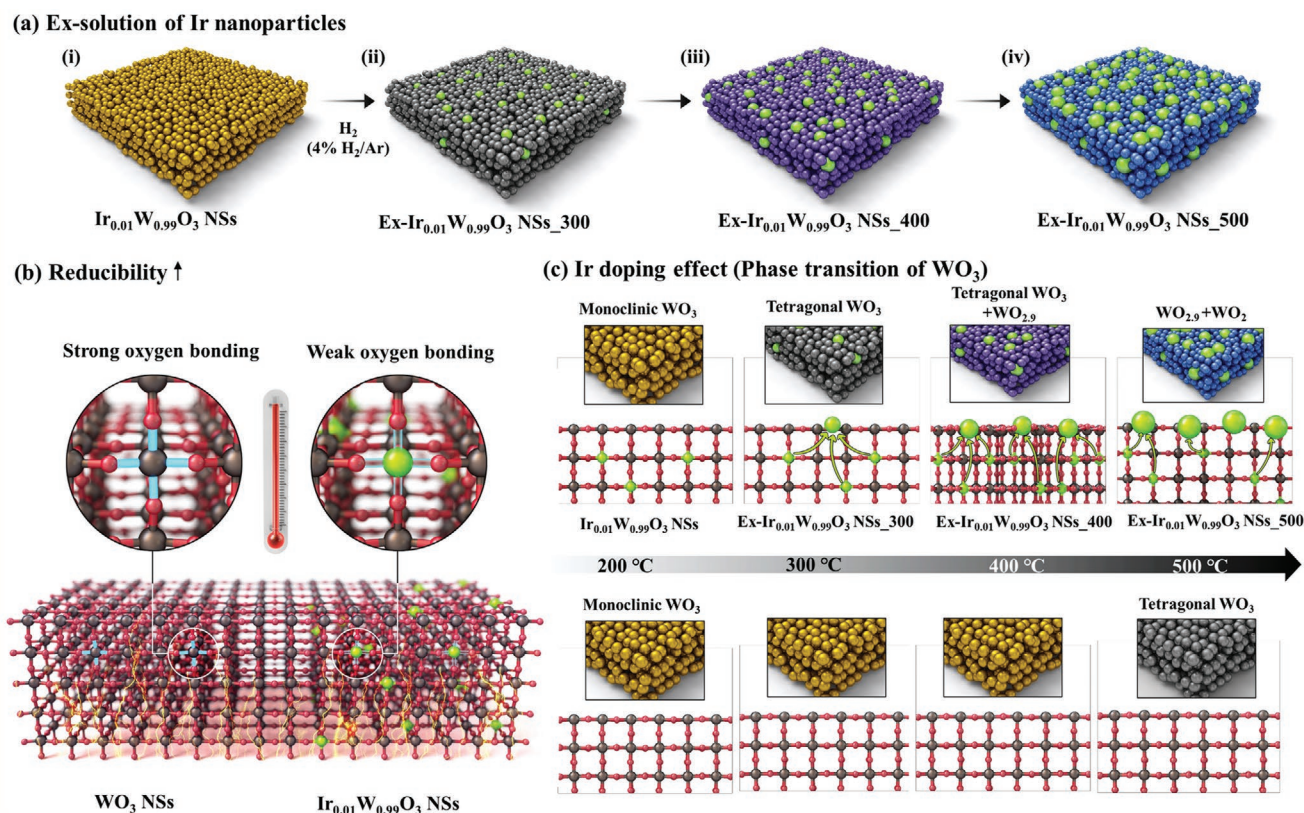


**Figure 1.** a–c) Schematics of the synthesis of ex-solved Ir nanoparticle (NP)-loaded WO<sub>3</sub> nanosheets (NSs) with various ex-solution conditions (a), the effect of Ir doping on the reducibility of Ir-doped WO<sub>3</sub> NSs (b), and the effect of Ir doping on the phase transitions of the WO<sub>3</sub> host oxide (c).

by intentionally depleting the A-site of the perovskite host with the chemical composition ABO<sub>3</sub> as a case study.<sup>[5]</sup> Jang et al. also controlled the energetics of Ni ex-solution by adjusting the lattice strain or surface crystal orientation of La<sub>0.2</sub>Sr<sub>0.7</sub>Ti<sub>0.9</sub>Ni<sub>0.1</sub>O<sub>3- $\delta$</sub>  epitaxial thin-film supports.<sup>[13]</sup> Notably, these attempts help elucidate the fundamentals of ex-solution phenomena, but their use is limited to only multicomponent systems beyond ternary (i.e., perovskite) or epitaxial thin films.<sup>[14]</sup>

Here, we present a new form of synergistic interactions between dopants and host binary oxides that can activate the ex-solution process. The addition of a transition metal dopant often increases the reducibility of the oxide lattice and therefore leads to a transition to a more oxygen-deficient phase. Such a transition may change the symmetry of the host oxide structure and destabilize the transition metal cations therein, resulting in the extrusion of the transition metals at the surface of the host oxide. To demonstrate this idea, we selected WO<sub>3</sub>, which shows multiple crystal structures according to the oxygen content and/or the surrounding conditions, as the model binary system, and we monitored how the oxide phases and surface morphologies changed as a function of Ir doping during the reduction process in real time. **Figure 1a** illustrates the experimental procedure. By controlling the reduction temperature from 300 to 500 °C, the crystalline structure of the host WO<sub>3</sub> and the size distribution of the ex-solved Ir particles were investigated. Unlike W, which has a +6 oxidation state in the WO<sub>3</sub> lattice and strongly binds to neighboring oxygen ions, Ir is a precious metal with weak interactions

with oxygen ions. Therefore, substituting Ir for W can improve the reducibility of WO<sub>3</sub> (Figure 1b) and facilitate phase transitions to more reduced crystal structures (Figure 1c). In this study, we observed how the phase transitions of WO<sub>3</sub> caused by the Ir dopant affect the Ir ex-solution process. These transitions greatly promote the formation of Ir NPs, and we successfully synthesized high-specific-area (14.99 m<sup>2</sup> g<sup>-1</sup>, Figure S1d, Supporting Information) WO<sub>3</sub> sheets uniformly decorated with Ir particles at temperatures of  $\approx$ 300 °C. To the best of our knowledge, this is the lowest-temperature-level heat treatment reported in the literature that can generate ex solution particles (Tables S1 and S2, Supporting Information), even when considering highly reducible elements (i.e., precious metals; Ru, Pd, Ag, Au, Pt, and Ir). In addition, this is the first successful ex-solution using WO<sub>3</sub>, which is a binary oxide material widely used in various industries such as sensors,<sup>[15]</sup> photocatalysts,<sup>[16]</sup> and supercapacitors.<sup>[17]</sup>

We synthesized Ir-doped WO<sub>3</sub> nanosheets (NSs) and then produced ex-solved Ir NPs on the surface of the sheets via reduction in a dilute H<sub>2</sub> (4% H<sub>2</sub>/Ar) atmosphere. The as-synthesized WO<sub>3</sub> NSs doped with 1 at% Ir (hereafter, Ir<sub>0.01</sub>W<sub>0.99</sub>O<sub>3</sub> NSs) were fabricated via a graphene oxide-nanocellulose (GONC) templating route (Figure S1a,b, Supporting Information).<sup>[18]</sup> 1D cellulose nanofibrils were bound to the surfaces of GO NSs to form net-like GONC composites (see the Experimental Section). The high storage capacity of cellulose for metal ions allowed the Ir (1 at%) and W (99 at%) precursors to be uniformly coated on the surface of GONC, and subsequent calcination at 600 °C

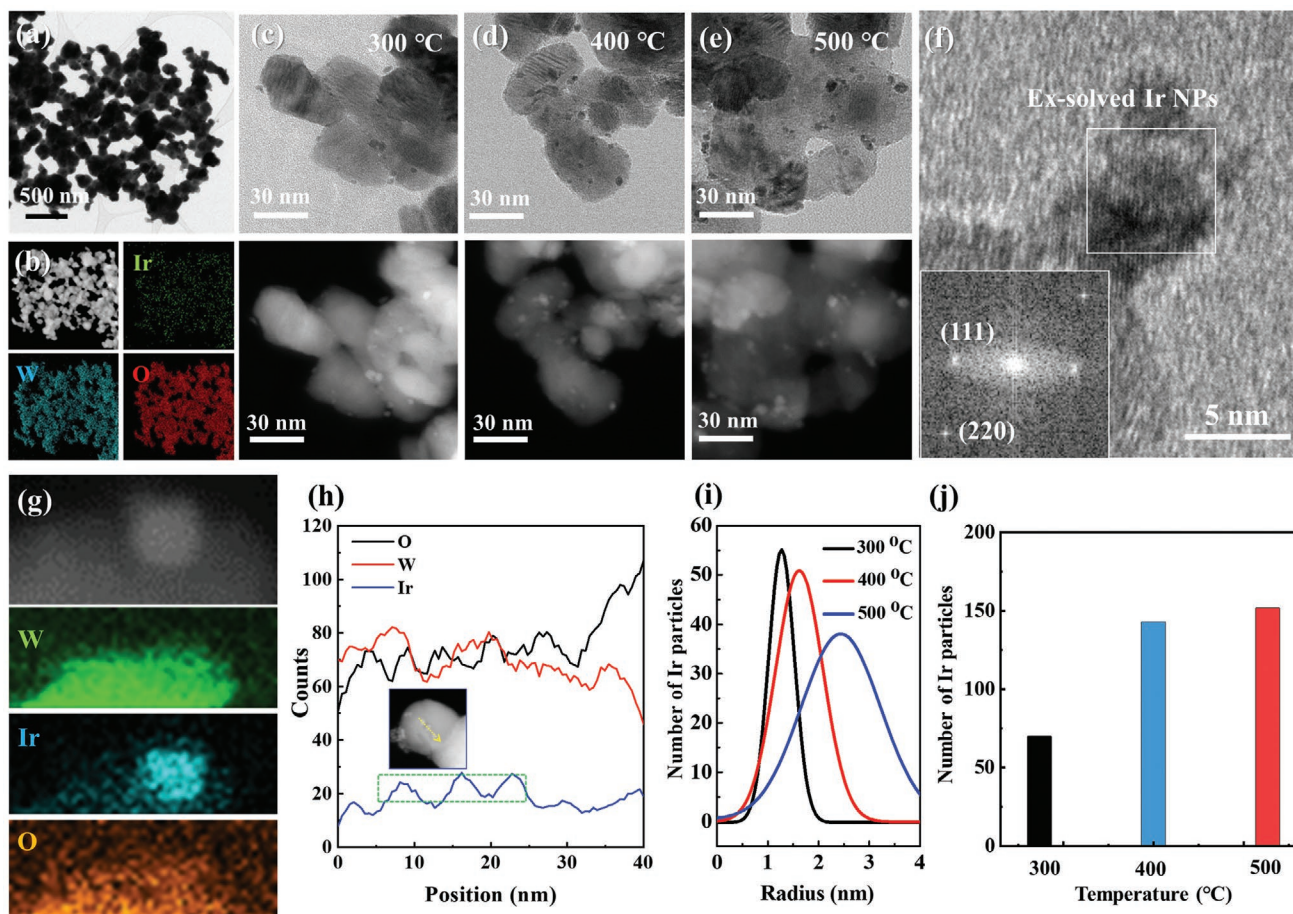


**Figure 2.** a) TEM image of  $\text{Ir}_{0.01}\text{W}_{0.99}\text{O}_3$  NSs. b) EDS elemental mapping analysis of  $\text{Ir}_{0.01}\text{W}_{0.99}\text{O}_3$  NSs. c–e) In situ TEM images of  $\text{Ir}_{0.01}\text{W}_{0.99}\text{O}_3$  NSs annealed in  $\text{H}_2/\text{Ar}$  (4%/96% volume ratio) at various temperatures: c) at 300 °C, Ex- $\text{Ir}_{0.01}\text{W}_{0.99}\text{O}_3$  NSs\_300; d) at 400 °C, Ex- $\text{Ir}_{0.01}\text{W}_{0.99}\text{O}_3$  NSs\_400; e) at 500 °C, Ex- $\text{Ir}_{0.01}\text{W}_{0.99}\text{O}_3$  NSs\_500; bottom panels: corresponding STEM images. f) HRTEM image of Ex- $\text{Ir}_{0.01}\text{W}_{0.99}\text{O}_3$  NSs\_400 with corresponding FFT pattern (inset). g) EDS elemental mapping analysis of Ex- $\text{Ir}_{0.01}\text{W}_{0.99}\text{O}_3$  NSs\_400. h) Data plots of the EDS line-scan of Ex- $\text{Ir}_{0.01}\text{W}_{0.99}\text{O}_3$  NSs\_400. i) Size distributions of ex-solved Ir nanoparticles at 300–500 °C. j) Number of ex-solved Ir nanoparticles at 300–500 °C.

in ambient air produced the targeted  $\text{Ir}_{0.01}\text{W}_{0.99}\text{O}_3$  NSs. Then, reductive annealing of the as-prepared  $\text{Ir}_{0.01}\text{W}_{0.99}\text{O}_3$  NSs at 300, 400, and 500 °C was conducted to form the ex-solved Ir NPs (refer to Figure 1). Considering the simple fabrication method of GONC, target catalytic materials or sensing materials were largely synthesized with high reliability and yields.<sup>[18]</sup>

Figure 2a shows a transmission electron microscopy (TEM) image of the as-prepared porous  $\text{Ir}_{0.01}\text{W}_{0.99}\text{O}_3$  NSs. The elements Ir, W, and O were evenly dispersed in the  $\text{Ir}_{0.01}\text{W}_{0.99}\text{O}_3$  NSs, as confirmed by energy-dispersive X-ray spectroscopy (EDS) (Figure 2b). Moreover, the X-ray diffraction (XRD) patterns of the NSs are consistent with the typical spectrum of a monoclinic  $\text{WO}_3$  crystalline structure without any secondary phase, which agrees with previous studies,<sup>[19]</sup> indicating that Ir was fully dissolved in the  $\text{WO}_3$  lattice (Figure S2, Supporting Information). These observations are consistent with the fact that the solubility of Ir in bulk monoclinic  $\text{WO}_3$  synthesized by conventional solid-state reactions is  $\approx 1$  at% (Figure S3a,b, Supporting Information).

Then, we observed the dynamic behaviors (i.e., the metal ex-solution and phase transition of the host oxides) of the NSs

under a reductive gas atmosphere (4%  $\text{H}_2/\text{Ar}$ ) at temperatures of 300, 400, and 500 °C using in situ TEM. The samples are named Ex- $\text{Ir}_{0.01}\text{W}_{0.99}\text{O}_3$  NSs\_300, Ex- $\text{Ir}_{0.01}\text{W}_{0.99}\text{O}_3$  NSs\_400, and Ex- $\text{Ir}_{0.01}\text{W}_{0.99}\text{O}_3$  NSs\_500 according to the reduction temperature. The surface morphology of Ex- $\text{Ir}_{0.01}\text{W}_{0.99}\text{O}_3$  NSs\_500 is shown in Figure S4 (Supporting Information). Ex-solved Ir particles were formed on the surface of the  $\text{WO}_3$  NSs. Moreover, Figure 2c–e presents bright-field (BF) images (upper side) and high-angle annular dark-field (HAADF) scanning transmission electron microscopy (STEM) images (bottom side) obtained during the in situ reduction processes. Under reducing conditions, nanosized particles (diameter < 5 nm) were ex-solved on the surfaces of the NSs above 300 °C (Figure 2c–e), which is the lowest temperature level among the ex-solution temperatures of various compounds reported to date (Tables S1 and S2, Supporting Information). The high-resolution TEM (HRTEM) image of an ex-solved particle obtained during the reduction process and the corresponding fast Fourier transform (FFT) pattern verify that the particle is metallic Ir with a face-centered cubic structure (Figure 2f).<sup>[20]</sup> However, when exposed to ambient air, the Ir NPs were partially oxidized, as

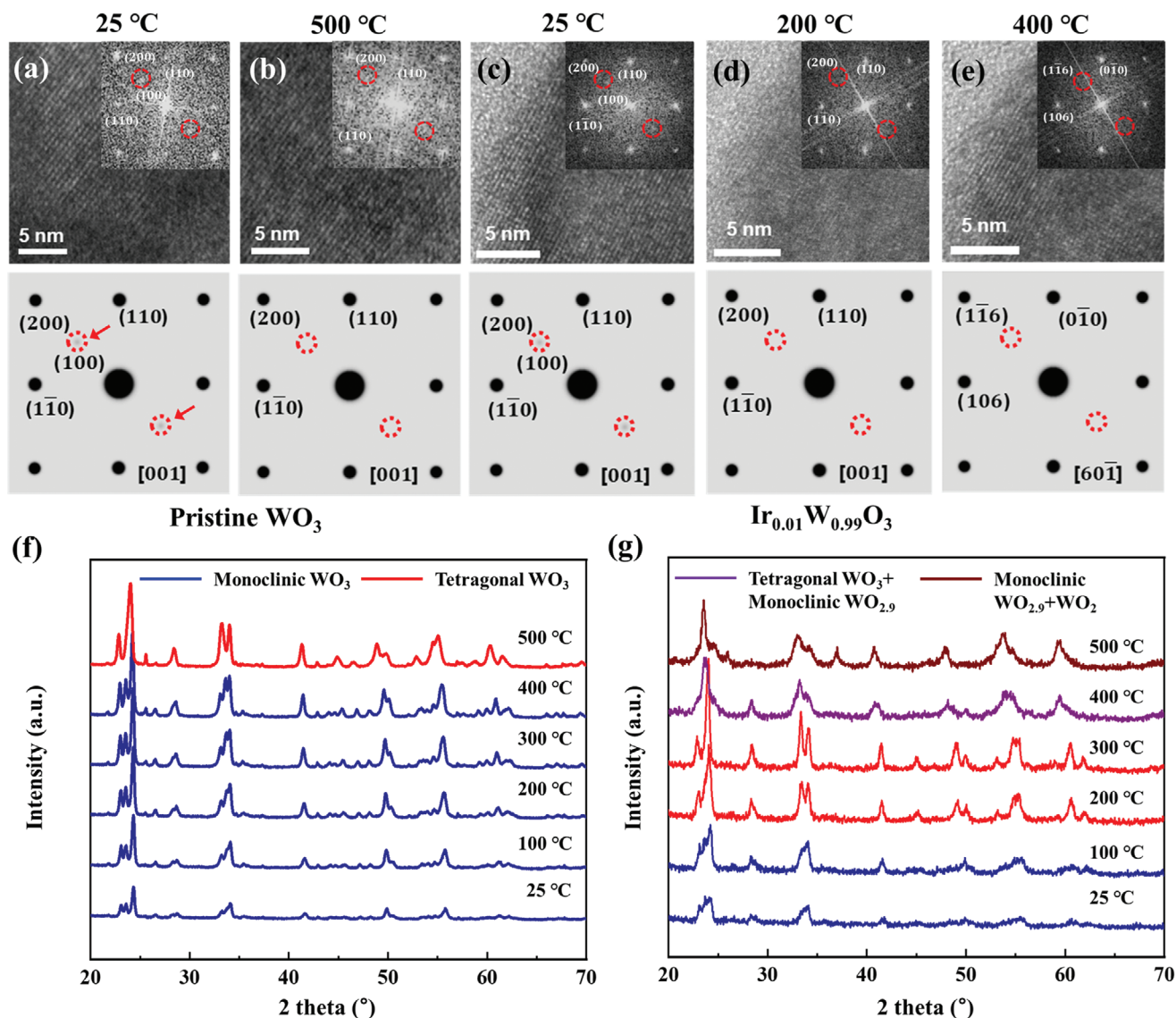


**Figure 3.** a–e) In situ TEM analysis in  $\text{H}_2/\text{Ar}$  (4%/96% volume ratio) with experimental fast Fourier transform (FFT) patterns (corresponding insets) and simulated FFT patterns of pristine  $\text{WO}_3$  NSs at a) 25 °C (a) and 500 °C (b), and  $\text{Ir}_{0.01}\text{W}_{0.99}\text{O}_3$  NSs at 25 °C (c), 200 °C (d), and 400 °C (e). f, g) In situ X-ray diffraction (XRD) patterns acquired at elevated temperatures in  $\text{H}_2/\text{Ar}$  (4%/96% volume ratio) for pristine  $\text{WO}_3$  NSs (f) and  $\text{Ir}_{0.01}\text{W}_{0.99}\text{O}_3$  NSs (g).

confirmed by HRTEM and FFT, which showed that the NP became  $\text{IrO}_2$  with a tetragonal structure (Figure S5, Supporting Information). EDS mapping and line scan clearly confirm that the ex-solved particles contain Ir (Figure 2g,h and see Figure S6 in the Supporting Information). Furthermore, direct measurements of the NPs in the areas in Figure 2c–e and others (per projected area of 300 000  $\text{nm}^2$  at each temperature) reveal that the size, density and total volume of the NPs increase with temperature (Figure 2i,j and Table S3, Supporting Information). These trends can be explained by the fact that the amount of ex-solution increases as the reduction temperature increases.<sup>[9]</sup> Furthermore, this ultralow-temperature ex-solution inhibits further sintering of the host oxide structure. Even after heat treatment at 500 °C, the Ir-ex-solved  $\text{WO}_3$  NSs had a specific surface area of 13.68  $\text{m}^2 \text{g}^{-1}$ , which is very similar to that (14.99  $\text{m}^2 \text{g}^{-1}$ )

of  $\text{Ir}_{0.01}\text{W}_{0.99}\text{O}_3$  NSs (Figure S7, Supporting Information). In addition to Ir component, we further examined that Pt and Pd elements can be also ex-solved on the surface of  $\text{WO}_3$  NSs with the same Ir ex-solution procedure (Figure S8, Supporting Information). This result demonstrates that our approach can be broadened to various catalytic noble metal components.

To investigate the phase transition of the host oxide, we carried out in situ TEM analysis. The HRTEM images and corresponding FFT patterns of pristine  $\text{WO}_3$  and  $\text{Ir}_{0.01}\text{W}_{0.99}\text{O}_3$  NSs were obtained during the reduction process (Figure 3a–e). The simulated FFT patterns are also shown to confirm the FFT patterns (bottom panels for Figure 3a–e). For pristine  $\text{WO}_3$  NSs (Figure 3a,b), monoclinic  $\text{WO}_3$  (m- $\text{WO}_3$ ) is converted to tetragonal  $\text{WO}_3$  (t- $\text{WO}_3$ ) at 500 °C, as verified by the disappearance of the (100) diffraction points in the FFT of m- $\text{WO}_3$  from

that of t-WO<sub>3</sub> (see the dotted red circles in Figure 3a,b). On the other hand, this phase transition takes place at ≈200 °C in Ir<sub>0.01</sub>W<sub>0.99</sub>O<sub>3</sub> NSs (Figure 3c,d), and this is followed by the evolution of the WO<sub>2.9</sub> phase at 400 °C, as identified by the FFT pattern of the generated phase (Figure 3e).

We also observed the change in crystal structure of the WO<sub>3</sub> samples by in situ XRD. Figure 3f,g shows the in situ XRD data of pristine WO<sub>3</sub> and Ir<sub>0.01</sub>W<sub>0.99</sub>O<sub>3</sub> NSs acquired while flowing H<sub>2</sub>/Ar (4%/96% volume ratio) gas in the temperature range of 25–500 °C. For pristine WO<sub>3</sub> NSs, the initial m-WO<sub>3</sub> phase remains up to 400 °C, and it transforms to the t-WO<sub>3</sub> phase at 500 °C (Figure 3f). In contrast, such a phase transition from m-WO<sub>3</sub> to t-WO<sub>3</sub> occurs at a much lower temperature (i.e., 200 °C) in Ir<sub>0.01</sub>W<sub>0.99</sub>O<sub>3</sub> NSs (see the red spectra in Figure 3g). As the temperature increases, the WO<sub>3</sub> NSs become more oxygen deficient; the WO<sub>2.9</sub> phase arises in a mixture with t-WO<sub>3</sub> at 400 °C (see the purple spectrum in Figure 3g), and the WO<sub>2</sub> phase is generated in the presence of the WO<sub>2.9</sub> phase at 500 °C (see the brown spectrum in Figure 3g and Figure S9, Supporting Information). Therefore, the results of in situ XRD and in situ TEM are consistent, indicating that the sequential phase transition of WO<sub>3</sub> occurs throughout the sample. We note that a WO<sub>2</sub> phase was not detected during in situ TEM measurements, probably due to the small amounts of this phase (WO<sub>2</sub>) and because they are not oriented along a particular zone axis, thereby preventing HRTEM imaging. We concluded that Ir doping facilitates the bulk phase transition of the WO<sub>3</sub> lattice. Since the nanosized host oxide structure was used, the diffusion length of the Ir cations was very short, so it could be expected that a larger amount of Ir would be formed on the surface of WO<sub>3</sub>. As shown in Figure S10d (Supporting Information), we deconvoluted the Ir 4f spectra into ionic Ir (Ir<sup>4+</sup>) and metallic Ir and compared the area of two states. As a result, the portion of metallic state of Ir (the proportion of ex-solved Ir) was estimated to be about 48% which is ex-solved Ir NPs on the surface of WO<sub>3</sub>.

In our experimental results, the required temperatures for the phase transition from m-WO<sub>3</sub> to t-WO<sub>3</sub> with and without Ir doping were ≈200 and 500 °C, respectively. To explain the different phase transition temperatures upon Ir doping, we compared the thermodynamic stability of pristine m-WO<sub>3</sub> and Ir-doped m-WO<sub>3</sub> with those of t-WO<sub>3</sub> phases. We defined the thermodynamic stability difference between the two phases as the phase transition energy (Figure 4a). The calculated phase transition energies per formula unit (f.u.) from m-WO<sub>3</sub> to t-WO<sub>3</sub> with and without Ir were –0.04 and 0.00 eV, respectively. For the phase transition from t-WO<sub>3</sub> to oxygen-deficient WO<sub>2.9</sub>, Ir-doped t-WO<sub>3</sub> showed a phase transition energy 0.08 eV lower (0.17 eV) than that of pristine t-WO<sub>3</sub> (0.25 eV). This indicates that Ir doping facilitates the 1st phase transition from m-WO<sub>3</sub> to t-WO<sub>3</sub> as well as the 2nd phase transition from t-WO<sub>3</sub> to oxygen-deficient WO<sub>2.9</sub>.

In the phase transition of Ir-doped m-WO<sub>3</sub> to t-WO<sub>3</sub> after 200 °C, Ir ex-solution started at 300 °C as the temperature increased (previous section, in situ XRD and TEM results). In particular, Ir ex-solution was significantly at 400 °C when the second phase transition occurred from t-WO<sub>3</sub> to WO<sub>2.9</sub> (i.e., the number density of Ir NPs increased two-fold, specifically, from 70 to 143, Table S3, Supporting Information). This implies that the phase transition to WO<sub>2.9</sub> provides an additional

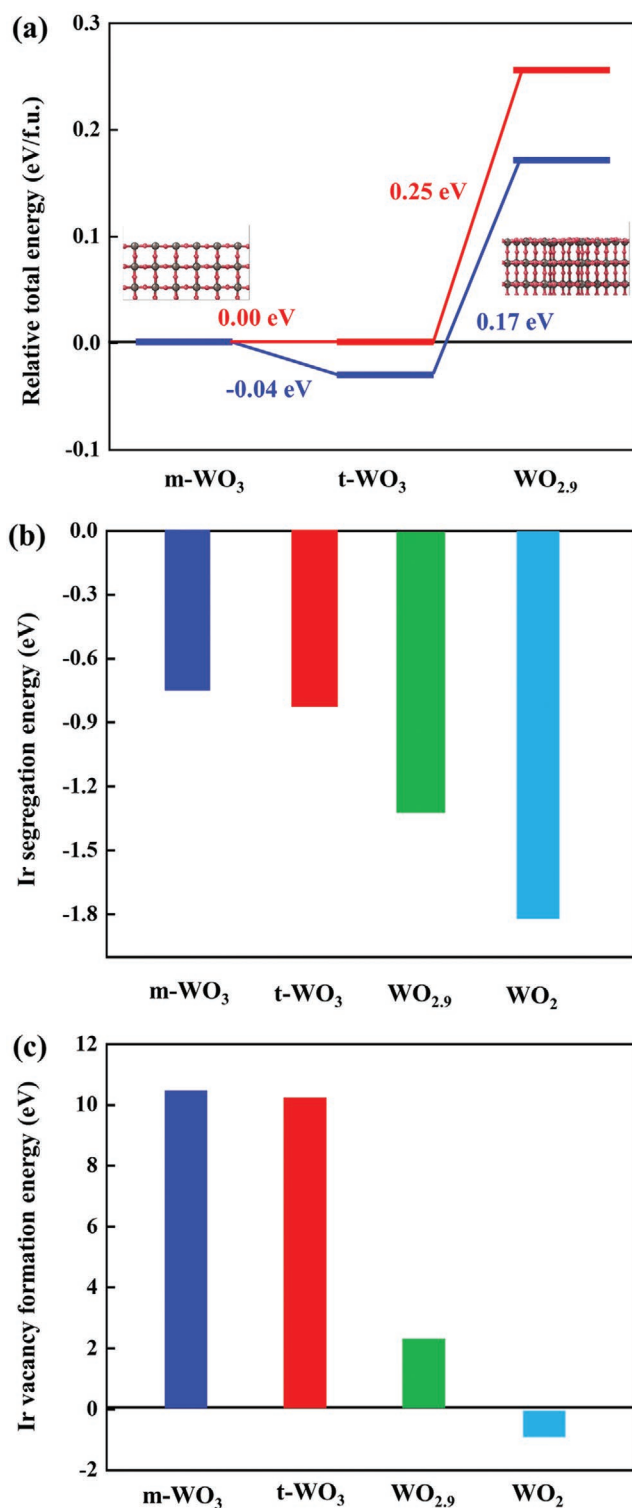


**Figure 4.** a) Relative total energy per formula unit from m-WO<sub>3</sub> to t-WO<sub>3</sub> and from t-WO<sub>3</sub> to oxygen-deficient WO<sub>2.9</sub> with/without Ir doping; b) Ir segregation energy on m-WO<sub>3</sub>, t-WO<sub>3</sub>, WO<sub>2.9</sub>, and WO<sub>2</sub>; c) Ir extraction energy on Ir-doped m-WO<sub>3</sub>, t-WO<sub>3</sub>, WO<sub>2.9</sub>, and WO<sub>2</sub>.

thermodynamic driving force for Ir ex-solution from the host structure. To form the ex-solved Ir NPs, Ir should be segregated at the surface of the oxide, so the segregation tendency of Ir is

an important indicator of Ir ex-solution. We thus calculated the Ir segregation energy ( $E_{\text{Ir-seg}}$ ) by comparing the total energies of systems when Ir was located at the surface and in the bulk using the slab models described in Figures S14 and S15 of the Supporting Information (Figure 4b). The calculated Ir segregation energies of m-WO<sub>3</sub>, t-WO<sub>3</sub>, and WO<sub>2.9</sub> were -0.73, -0.76, and -1.26 eV, respectively, which supports that Ir easily segregates at the surface in the more oxygen-deficient phases. Thus, the simulation results demonstrate that the Ir ex-solution was highly promoted by the phase transition of WO<sub>3</sub>.

To investigate the cause of the decrease in  $E_{\text{Ir-seg}}$  during the reduction of WO<sub>3</sub>, we calculated the Ir vacancy formation energy ( $E_{\text{Ir-vac}}$ ) on m-WO<sub>3</sub>, t-WO<sub>3</sub>, and WO<sub>2.9</sub>, which was defined as how much energy is required to extract Ir from each host lattice (Figure 4c). Lower  $E_{\text{Ir-vac}}$  values indicate that Ir is weakly bound to the surrounding lattice oxygen ions, and thus, it could be easily ex-solved from the host structure. The  $E_{\text{Ir-vac}}$  on the host structures of m-WO<sub>3</sub>, t-WO<sub>3</sub>, and WO<sub>2.9</sub> were 10.31, 10.25, and 2.21 eV, respectively. Interestingly, WO<sub>2.9</sub> has a significantly lower  $E_{\text{Ir-vac}}$  than do m-WO<sub>3</sub> and t-WO<sub>3</sub>. The elongation of the Ir–O bond in WO<sub>2.9</sub> (2.02 Å) compared to those in m-WO<sub>3</sub> (1.92 Å) or t-WO<sub>3</sub> (1.92 Å) implies that the Ir–O bond strength is decreased by the phase transition of WO<sub>3</sub> to WO<sub>2.9</sub>, and more space is available for Ir atoms to segregate toward the surface. Only when Ir was doped was the further transition of WO<sub>2.9</sub> to WO<sub>2</sub> also observed in our in situ XRD experiments. Both  $E_{\text{Ir-seg}}$  (-1.81 eV) and  $E_{\text{Ir-vac}}$  (-0.77 eV) for WO<sub>2</sub> with its elongated Ir–O bond (2.06 Å) are much lower than  $E_{\text{Ir-seg}}$  (-1.26 eV) and  $E_{\text{Ir-vac}}$  (2.21 eV) of WO<sub>2.9</sub>, indicating that the reduction of WO<sub>3</sub> to WO<sub>2.9</sub> or to WO<sub>2</sub> can significantly improve Ir ex-solution. In summary, our DFT results demonstrated that Ir plays an important role in the phase transition of m-WO<sub>3</sub> to t-WO<sub>3</sub> to WO<sub>2.9</sub>. In addition, the phase transition facilitates Ir segregation from the lattice of the host oxide due to the low stability of Ir in low oxygen-containing WO<sub>3</sub> (WO<sub>3-x</sub>) structures.

Last, we demonstrate the potential suitability of the Ir-exsolved WO<sub>3</sub> NSs as highly sensitive and reliable gas-sensing layers. To date, most ex-solution processes have been applied to high-temperature operating systems such as solid oxide fuel cells and three-way catalysts.<sup>[21]</sup> On the other hand, only a few attempts at producing ex-solved catalyst-oxide systems, i.e., PdO, which is reoxidized from Pd NPs ex-solved on a perovskite-type sensing layer, and ex-solved the nonstoichiometric perovskite LaFePd<sub>0.05</sub>O<sub>3+x</sub> host oxide for impedance metric NO<sub>2</sub> sensor applications<sup>[22]</sup> have been reported. However, due to the unwanted particle growth originating from the high ex-solution processing temperature (≈700 °C) and high calcination temperature of perovskite host oxides (≈900 °C), enhanced sensing characteristics are difficult to achieve. To address these critical issues, we first designed a low-temperature ex-solution of Ir NPs on a nanoscale binary oxide system (e.g., WO<sub>3</sub> NSs). Due to the very low-temperature ex-solution process, a porous host structure with a high specific surface area (≈15 m<sup>2</sup> g<sup>-1</sup>) could be stably maintained while significantly improving the chemical sensing performance.

Since hydrogen sulfide (H<sub>2</sub>S) gas, which is an exhaled breath biomarker for halitosis and a harmful toxic gas, has a high affinity for metallic phases due to the strong chelation between sulfuric compounds and the noble metals,<sup>[23]</sup> we compared the

H<sub>2</sub>S sensing characteristics of the as-prepared 4 samples (e.g., Ir<sub>0.01</sub>W<sub>0.99</sub>O<sub>3</sub> NSs, Ex-Ir<sub>0.01</sub>W<sub>0.99</sub>O<sub>3</sub> NSs<sub>300</sub>, Ex-Ir<sub>0.01</sub>W<sub>0.99</sub>O<sub>3</sub> NSs<sub>400</sub>, and Ex-Ir<sub>0.01</sub>W<sub>0.99</sub>O<sub>3</sub> NSs<sub>500</sub>). Four as-prepared samples were uniformly coated on the sensor substrates with an interdigitated Au sensing electrode (width = 25 μm, gap size = 150 μm), and the fabricated sensors were exposed to controlled concentrations of gases (e.g., H<sub>2</sub>S, CH<sub>3</sub>SH, C<sub>3</sub>H<sub>6</sub>O, C<sub>7</sub>H<sub>8</sub>, CO, NH<sub>3</sub>, and HCHO) (see the Experimental Section). As shown in Figure 5a, the ex-solved Ir<sub>0.01</sub>W<sub>0.99</sub>O<sub>3</sub> NS sensor showed a significantly better H<sub>2</sub>S sensing response compared to that of Ir<sub>0.01</sub>W<sub>0.99</sub>O<sub>3</sub> NSs. Ex-Ir<sub>0.01</sub>W<sub>0.99</sub>O<sub>3</sub> NSs<sub>400</sub> showed the highest H<sub>2</sub>S response ( $R_{\text{air}}/R_{\text{gas}} = 35 @ 5 \text{ ppm H}_2\text{S}$ , 375 °C, over 10-fold higher response than Ir<sub>0.01</sub>W<sub>0.99</sub>O<sub>3</sub> NSs ( $R_{\text{air}}/R_{\text{gas}} = 2.91 @ 5 \text{ ppm}$ )). Very surprisingly, the ex-solution effects in Ir<sub>0.01</sub>W<sub>0.99</sub>O<sub>3</sub> NSs further contributed to its enhanced selectivity toward H<sub>2</sub>S (Figure 5b,c). Ex-Ir<sub>0.01</sub>W<sub>0.99</sub>O<sub>3</sub> NSs<sub>400</sub> showed much higher H<sub>2</sub>S response and superior selectivity toward H<sub>2</sub>S molecules compared to Ir<sub>0.01</sub>W<sub>0.99</sub>O<sub>3</sub> NSs. This result indicates that ex-solved Ir nanocatalysts dominantly contribute to the dramatic improvement of H<sub>2</sub>S sensing behaviors (Figure S11, Supporting Information). The Ir<sub>0.01</sub>W<sub>0.99</sub>O<sub>3</sub> NSs showed poor selectivity for 5 ppm H<sub>2</sub>S, while Ex-Ir<sub>0.01</sub>W<sub>0.99</sub>O<sub>3</sub> NSs<sub>400</sub> showed dramatically improved H<sub>2</sub>S selectivity with negligible responses to the other gas species ( $R_{\text{air}}/R_{\text{gas}} < 5$  to 5 ppm CH<sub>3</sub>SH, C<sub>3</sub>H<sub>6</sub>O, C<sub>7</sub>H<sub>8</sub>, CO, NH<sub>3</sub>, and HCHO). The optimal H<sub>2</sub>S sensing behavior was observed at 375 °C based on temperature-dependent H<sub>2</sub>S sensing performances (Figure 5d). According to previous literature, ex-solved NPs exhibit excellent sintering and coking resistance due to their socketing geometry.<sup>[8,24]</sup> Likewise, Ex-Ir<sub>0.01</sub>W<sub>0.99</sub>O<sub>3</sub> NSs<sub>400</sub> maintained its stable H<sub>2</sub>S sensing characteristics during long H<sub>2</sub>S sensing cycles (>80 cycles), while WO<sub>3</sub> NSs decorated with Ir NPs, which was synthesized by the conventional polyol method,<sup>[25]</sup> showed severe fluctuations during repetitive H<sub>2</sub>S sensing, resulting in poor long-term stability (Figure 5e).

To further demonstrate the material stability of long-cycled Ex-Ir<sub>0.01</sub>W<sub>0.99</sub>O<sub>3</sub> NSs, i.e., 82 repeated H<sub>2</sub>S exposures, we carried out ex situ XRD and TEM analyses. As shown in the XRD patterns in Figure 5f, the host oxides for Ex-Ir<sub>0.01</sub>W<sub>0.99</sub>O<sub>3</sub> NSs<sub>300</sub>, Ex-Ir<sub>0.01</sub>W<sub>0.99</sub>O<sub>3</sub> NSs<sub>400</sub>, and Ex-Ir<sub>0.01</sub>W<sub>0.99</sub>O<sub>3</sub> NSs<sub>500</sub> (t-WO<sub>3</sub>, t-WO<sub>3</sub>+WO<sub>2.9</sub>, and WO<sub>2.9</sub>+WO<sub>2</sub>, respectively) were reconverted to the m-WO<sub>3</sub> phase after sensing at an operating temperature (375 °C) (magnified region of Figure 5f and Figure S12, Supporting Information). Moreover, ex situ TEM analysis clearly indicated that ex-solved Ir NPs with sizes of 1–3 nm remained on the WO<sub>3</sub> NSs even after 82 sensing cycles (Figure 5g,h). Furthermore, EDS mapping analysis with dark field TEM showed that ex-solved Ir NPs existed after numerous sensing cycles (Figure 5i). Since ex-solved catalytic NPs on oxide supports showed ultrahigh stability even under harsh gas-sensing conditions (e.g., exposure to toxic and hazardous reducing gases), our scientific findings (e.g., the Ir dopant triggering an accelerated phase transformation of host WO<sub>3</sub> and facilitating more effective Ir ex-solution) will be applied to highly reliable, stable, and selective chemical sensing platforms such as those in harmful gas monitoring and health-care based on exhaled breath molecule detection.<sup>[26]</sup> In addition to gas-sensing characteristics, we investigated the feasibility of ex-solved Ir NPs on WO<sub>3</sub> NSs as catalysts in chemical gas conversion. Carbon monoxide oxidation ( $\text{CO} + \frac{1}{2}\text{O}_2 = \text{CO}_2$ ) was

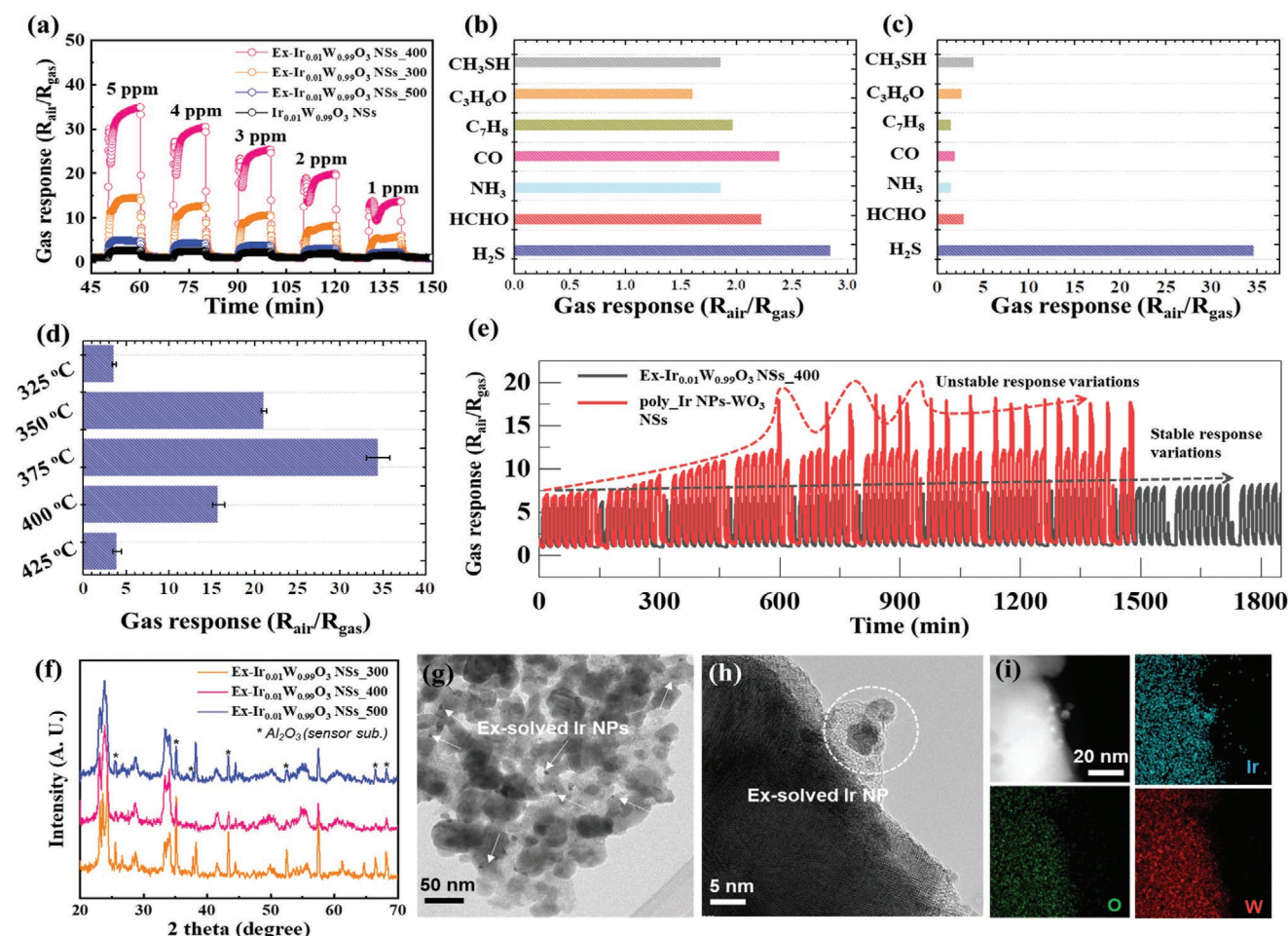


**Figure 5.** a) Dynamic  $\text{H}_2\text{S}$  response transitions of  $\text{Ir}_{0.01}\text{W}_{0.99}\text{O}_3$  NSs, Ex- $\text{Ir}_{0.01}\text{W}_{0.99}\text{O}_3$  NSs\_300, Ex- $\text{Ir}_{0.01}\text{W}_{0.99}\text{O}_3$  NSs\_400, and Ex- $\text{Ir}_{0.01}\text{W}_{0.99}\text{O}_3$  NSs\_500. b, c) Selective gas-sensing characteristics of  $\text{Ir}_{0.01}\text{W}_{0.99}\text{O}_3$  (b) and Ex- $\text{Ir}_{0.01}\text{W}_{0.99}\text{O}_3$  NSs\_400 (c). d) Temperature-dependent  $\text{H}_2\text{S}$  sensing response of Ex- $\text{Ir}_{0.01}\text{W}_{0.99}\text{O}_3$  NSs\_400. e) Cyclic sensing response of Ex- $\text{Ir}_{0.01}\text{W}_{0.99}\text{O}_3$  NSs\_400 and Ir-NPs-decorated  $\text{WO}_3$  NSs at 1 ppm  $\text{H}_2\text{S}$ . f) Ex situ X-ray diffraction (XRD) patterns of Ex- $\text{Ir}_{0.01}\text{W}_{0.99}\text{O}_3$  NSs\_300, Ex- $\text{Ir}_{0.01}\text{W}_{0.99}\text{O}_3$  NSs\_400, and Ex- $\text{Ir}_{0.01}\text{W}_{0.99}\text{O}_3$  NSs\_500 after  $\text{H}_2\text{S}$  sensing tests. g, h) Ex situ TEM analysis of Ex- $\text{Ir}_{0.01}\text{W}_{0.99}\text{O}_3$  NSs\_400 after  $\text{H}_2\text{S}$  sensing tests. i) EDS elemental mapping analysis of Ex- $\text{Ir}_{0.01}\text{W}_{0.99}\text{O}_3$  NSs\_400 after  $\text{H}_2\text{S}$  sensing tests.

selected as a model gas conversion reaction because the CO oxidation reaction is one of the most representative combustion processes. The  $\text{Ir}_{0.01}\text{W}_{0.99}\text{O}_3$  NSs before the ex-solution reaction show only 20% CO conversion at 400 °C (Figure S16a, Supporting Information). In contrast,  $\text{Ir}_{0.01}\text{W}_{0.99}\text{O}_3$  NSs after ex-solution exhibit nearly 100% CO conversion at 300 °C regardless of the ex-solution temperature. This result demonstrates that low-temperature ex-solution triggered by phase transformation of host oxides can be a universal and versatile processing platform to provide highly robust heterogeneous catalysts for various applications.

In summary, we rationally designed uniformly distributed metallic NPs (e.g., Ir) on a binary host oxide (i.e.,  $\text{WO}_3$ ) with a NS structure via an ultralow-temperature ex-solution process ( $\approx 300$  °C). An extremely low ex-solution temperature was achieved through two factors: i) Ir doping drives the dynamic phase transition of host  $\text{WO}_3$  during the ex-solution process, and ii) ex-solution of the Ir particles at the oxide surface is accelerated by the phase transition of host  $\text{WO}_3$ . Such a cogwheel-like relationship between doping, phase transition, and

ex-solution enables the formation of metallic Ir NPs without any noticeable sintering between the parent  $\text{WO}_3$  nanoparticles consisting of NSs, which is essential for maintaining highly porous and structurally stable morphologies as well as outstanding catalytic activity. The fine distribution and strong attachment of the Ir NPs to the host oxide enabled outstanding  $\text{H}_2\text{S}$  sensing performances with high selectivity and remarkably improved durability. In conclusion, the strategy described in this study suggests a new research direction that extends the current paradigm of ex-solved catalyst design.

## Experimental Section

**Sample Preparation:** Graphene oxide (GO) solution (1.2 mL, 5 mg  $\text{mL}^{-1}$ ) and 10 mL of aqueous tunicin (nanocellulose) solution (Tuni-GO sol) were mixed in a vial and vigorously stirred with a magnetic stirring bar at 300 rpm for 30 min. Then 0.123 g of tungsten precursor (ammonium metatungstate hydrate ( $(\text{NH}_4)_6\text{H}_2\text{W}_{12}\text{O}_{40}$ )) and 1.5 mg of iridium chloride hydrate ( $\text{IrCl}_3 \cdot x\text{H}_2\text{O}$ ) were spontaneously dissolved

in 24 mL of deionized water (DI water) (W/Ir sol) in a glass vial. The as-prepared W/Ir sol was added to the Tuni-GO sol (W/Ir\_Tuni-GO sol) and vigorously mixed at 300 rpm for 3 h. After this mixing process, the W/Ir\_Tuni-GO sol was centrifuged at 9000 rpm for 10 min, and the pellet of the centrifuged W/Ir\_Tuni-GO sol was dried at 50 °C for 6 h. The calcination process was conducted with a gel-like W/Ir\_Tuni-GO sol at 600 °C for 3 h with a ramping rate of 5 °C/min. After calcination, 1 at% Ir-doped WO<sub>3</sub> nanosheets (Ir<sub>0.01</sub>W<sub>0.99</sub>O<sub>3</sub> NSs) were obtained. To conduct the ex-solution process with Ir<sub>0.01</sub>W<sub>0.99</sub>O<sub>3</sub> NSs, additional calcinations at various temperatures (300, 400, and 500 °C) were performed under a reducing atmosphere (H<sub>2</sub>/Ar = 4/96%, v/v) for 1 h.

**DFT Calculations:** DFT calculations were performed to investigate the effects of Ir on the phase transition of WO<sub>3</sub> and Ir ex-solution using the Vienna ab initio Simulation Package (VASP).<sup>[27]</sup> Exchange-correlation effects were treated using the Perdew–Burke–Ernzerhof (PBE) functional based on the generalized gradient approximation (GGA).<sup>[28]</sup> A plane-wave was expanded with a cutoff of 400 eV. Monoclinic WO<sub>3</sub> (m-WO<sub>3</sub>), tetragonal WO<sub>3</sub> (t-WO<sub>3</sub>), WO<sub>2,9</sub>, and WO<sub>2</sub> were constructed using the crystal structures observed in our XRD results. The optimized structure parameters are listed in Table S4 (Supporting Information). More calculation details are provided in the Supporting Information.

**Gas Sensing and CO Conversion Measurements:** The gas-sensing characteristics of the as-prepared materials were evaluated by dynamic resistance variations (response =  $R_{\text{air}}/R_{\text{gas}}$ ) during gas on/off cycles. To fabricate the sensing devices, the chemiresistive sensing powders (e.g., Ir<sub>0.01</sub>W<sub>0.99</sub>O<sub>3</sub> NSs and Ex-Ir<sub>0.01</sub>W<sub>0.99</sub>O<sub>3</sub> NSs) were dispersed in ethanol with ultrasonication. Then, the chemiresistive sensing materials (e.g., Ir<sub>0.01</sub>W<sub>0.99</sub>O<sub>3</sub> NSs and Ex-Ir<sub>0.01</sub>W<sub>0.99</sub>O<sub>3</sub> NSs) were separately drop-coated onto Al<sub>2</sub>O<sub>3</sub> sensing substrates (2.5 mm × 2.5 mm size) with interdigitated gold electrodes (width = 25 μm, gap size = 150 μm) for measuring the resistance variations. All of the sensors were stabilized in dry air (30% RH), and all the sensors were exposed to various gas molecules (CH<sub>3</sub>SH, C<sub>3</sub>H<sub>6</sub>O, C<sub>7</sub>H<sub>8</sub>, CO, NH<sub>3</sub>, HCHO, and H<sub>2</sub>S) at concentrations ranging from 1 to 5 ppm. Note that the gas on/off interval time was 10 min.

All CO conversion catalytic tests were conducted with a fixed-bed quartz flow microreactor with an internal diameter of 4 mm. To build a catalytic bed, 15 mg of catalyst mixed with 50 mg of silica beads was loaded into a quartz reactor. For the carbon monoxide oxidation test, the reactant gas mixture, consisting of 1 vol% CO, 2 vol% O<sub>2</sub>, and 97 vol% Ar, was fed at a rate of 50 mL min<sup>-1</sup>. After pretreating the samples in air pretreated at 300 °C to remove the surface adsorbates, the light-off curve was acquired at a ramping rate of 3 °C min<sup>-1</sup> between 30 and 400 °C. The reactant and product gases were monitored using a quadrupole mass spectrometer (MS, Pfeiffer Vacuum, GSD320) in real time using QUADERA software. The CO conversion ratio was calculated according to the following equation

$$\text{CO conversion (\%)} = \left( \frac{[\text{CO}]_{\text{in}} - [\text{CO}]_{\text{out}}}{[\text{CO}]_{\text{in}}} \right) \times 100 \quad (1)$$

## Supporting Information

Supporting Information is available from the Wiley Online Library or from the author.

## Acknowledgements

This work was supported by Samsung Research Funding & Incubation Center of Samsung Electronics under Project Number SRFC-MA1502-52.

## Conflict of Interest

The authors declare no conflict of interest.

## Author Contributions

J.-S.J. and J.K.K. contributed equally to this work. J.-S.J., J.K.K., B.-J.K., J.W.H., W.J., and I.-D.K. conceived the idea for this study. J.-S.J., J.K.K., and S.K. performed overall materials preparation, sensor fabrication, and characterization. W.-G.J. and B.-J.K. conducted in situ TEM analysis. J.-S.J. and D.-H.K. analyzed the gas-sensing results. J.H., K.K., and C.L. performed the DFT calculations. I.-D.K., W.J., J.H., and B.-J.K. supervised the project and wrote the manuscript. All authors contributed for the manuscript preparation by comments and discussion.

## Keywords

binary oxides, catalysts, ex-solution, host oxides, metal nanoparticles, phase transitions

Received: June 11, 2020

Revised: August 12, 2020

Published online: October 1, 2020

- [1] N. Zheng, G. D. Stucky, *J. Am. Chem. Soc.* **2006**, *128*, 14278.
- [2] J.-S. Jang, W.-T. Koo, S.-J. Choi, I.-D. Kim, *J. Am. Chem. Soc.* **2017**, *139*, 11868.
- [3] C. Kim, J.-W. Jung, K. R. Yoon, D.-Y. Youn, S. Park, I.-D. Kim, *ACS Nano* **2016**, *10*, 11317.
- [4] Y. Yao, Z. Huang, P. Xie, S. D. Lacey, R. J. Jacob, H. Xie, F. Chen, A. Nie, T. Pu, M. Rehwoldt, *Science* **2018**, *359*, 1489.
- [5] D. Neagu, G. Tsekouras, D. N. Miller, H. Ménard, J. T. Irvine, *Nat. Chem.* **2013**, *5*, 916.
- [6] J. H. Kim, J. K. Kim, H. G. Seo, D. K. Lim, S. J. Jeong, J. Seo, J. Kim, W. Jung, *Adv. Funct. Mater.* **2020**, *30*, 2001326.
- [7] a) J. K. Kim, Y.-R. Jo, S. Kim, B. Koo, J. H. Kim, B.-J. Kim, W. Jung, *Interfaces* **2020**, *12*, 24039; b) K. Kim, B. Koo, Y.-R. Jo, S. Lee, J. K. Kim, B.-J. Kim, W. Jung, J. W. Han, *Energy Environ. Sci.*, <https://doi.org/10.1039/d0ee01308k>.
- [8] D. Neagu, T.-S. Oh, D. N. Miller, H. Ménard, S. M. Bukhari, S. R. Gamble, R. J. Gorte, J. M. Vohs, J. T. Irvine, *Nat. Commun.* **2015**, *6*, 8120.
- [9] Y.-R. Jo, B. Koo, M.-J. Seo, J. K. Kim, S. Lee, K. Kim, J. W. Han, W. Jung, B.-J. Kim, *J. Am. Chem. Soc.* **2019**, *141*, 6690.
- [10] a) Z. Cao, L. Fan, G. Zhang, K. Shao, C. He, Q. Zhang, Z. Lv, B. Zhu, *Catal. Today* **2019**, *330*, 217; b) Y. Gao, D. Chen, M. Saccoccio, Z. Lu, F. Ciucci, *Nano Energy* **2016**, *27*, 499.
- [11] X. Hu, K. Xie, *J. Power Sources* **2019**, *430*, 20.
- [12] K.-Y. Lai, A. Manthiram, *Chem. Mater.* **2018**, *30*, 2515.
- [13] a) K. J. Kim, H. Han, T. Defferriere, D. Yoon, S. Na, S. J. Kim, A. M. Dayaghi, J. Son, T.-S. Oh, H. M. Jang, *J. Am. Chem. Soc.* **2019**, *141*, 7509; b) H. Han, J. Park, S. Y. Nam, K. J. Kim, G. M. Choi, S. S. Parkin, H. M. Jang, J. T. Irvine, *Nat. Commun.* **2019**, *10*, 1471.
- [14] C. Lin, A. C. Foucher, Y. Ji, C. D. Curran, E. A. Stach, S. McIntosh, R. J. Gorte, *ACS Catal.* **2019**, *9*, 7318.
- [15] Y. Zou, X. Zhou, Y. Zhu, X. Cheng, D. Zhao, Y. Deng, *Acc. Chem. Res.* **2019**, *52*, 714.
- [16] A. Tanaka, K. Hashimoto, H. Kominami, *J. Am. Chem. Soc.* **2014**, *136*, 586.
- [17] X. Lu, T. Zhai, X. Zhang, Y. Shen, L. Yuan, B. Hu, L. Gong, J. Chen, Y. Gao, J. Zhou, *Adv. Mater.* **2012**, *24*, 938.
- [18] J.-S. Jang, S. Cho, H. J. Han, S.-W. Song, S.-J. Kim, W.-T. Koo, D.-H. Kim, H. Jeong, Y. S. Jung, I. D. Kim, *ACS Appl. Mater. Interfaces* **2019**, *11*, 34100.
- [19] S.-J. Kim, S.-J. Choi, J.-S. Jang, N.-H. Kim, M. Hakim, H. L. Tuller, I.-D. Kim, *ACS Nano* **2016**, *10*, 5891.

- [20] L. Schick, R. Sanchis, V. González-Alfaro, S. Agouram, J. M. López, L. Torrente-Murciano, T. Garcia, B. Solsona, *Chem. Eng. J.* **2019**, 366, 100.
- [21] a) P. Littlewood, X. Xie, M. Bernicke, A. Thomas, R. Schomäcker, *Catal. Today* **2015**, 242, 111; b) Y. Zhu, W. Zhou, R. Ran, Y. Chen, Z. Shao, M. Liu, *Nano Lett.* **2016**, 16, 512.
- [22] X. Li, L. Dai, Z. He, W. Meng, Y. Li, L. Wang, *Sens. Actuators, B* **2019**, 298, 126827.
- [23] J. S. Jang, S. Yu, S. J. Choi, S. J. Kim, W. T. Koo, I. D. Kim, *Small* **2016**, 12, 5989.
- [24] N. W. Kwak, S. J. Jeong, H. G. Seo, S. Lee, Y. Kim, J. K. Kim, P. Byeon, S.-Y. Chung, W. Jung, *Nat. Commun.* **2018**, 9, 4829.
- [25] Y. Hajar, H. A. E. Dole, M. Couillard, E. A. Baranova, *ECS Trans.* **2016**, 72, 161.
- [26] S.-J. Kim, S.-J. Choi, J.-S. Jang, H.-J. Cho, I.-D. Kim, *Acc. Chem. Res.* **2017**, 50, 1587.
- [27] G. Kresse, J. Furthmüller, *Phys. Rev. B* **1996**, 54, 11169.
- [28] J. P. Perdew, K. Burke, M. Ernzerhof, *Phys. Rev. Lett.* **1996**, 77, 3865.